LETTER

A direct localization of a fast radio burst and its host

S. Chatterjee[1], C. J. Law[2], R. S. Wharton[1], S. Burke-Spolaor[3,4,5], J. W. T. Hessels[6,7], G. C. Bower[8], J. M. Cordes[1], S. P. Tendulkar[9], C. G. Bassa[6], P. Demorest[3], B. J. Butler[3], A. Seymour[10], P. Scholz[11], M. W. Abruzzo[12], S. Bogdanov[13], V. M. Kaspi[9], A. Keimpema[14], T. J. W. Lazio[15], B. Marcote[14], M. A. McLaughlin[4,5], Z. Paragi[14], S. M. Ransom[16], M. Rupen[11], L. G. Spitler[17] & H. J. van Langevelde[14,18]

Fast radio bursts[1,2] are astronomical radio flashes of unknown physical nature with durations of milliseconds. Their dispersive arrival times suggest an extragalactic origin and imply radio luminosities that are orders of magnitude larger than those of all known short-duration radio transients[3]. So far all fast radio bursts have been detected with large single-dish telescopes with arcminute localizations, and attempts to identify their counterparts (source or host galaxy) have relied on the contemporaneous variability of field sources[4] or the presence of peculiar field stars[5] or galaxies[4]. These attempts have not resulted in an unambiguous association[6,7] with a host or multi-wavelength counterpart. Here we report the subarcsecond localization of the fast radio burst FRB 121102, the only known repeating burst source[8-11], using high-time-resolution radio interferometric observations that directly image the bursts. Our precise localization reveals that FRB 121102 originates within 100 milliarcseconds of a faint 180-microJansky persistent radio source with a continuum spectrum that is consistent with non-thermal emission, and a faint (twenty-fifth magnitude) optical counterpart. The flux density of the persistent radio source varies by around ten per cent on day timescales, and very long baseline radio interferometry yields an angular size of less than 1.7 milliarcseconds. Our observations are inconsistent with the fast radio burst having a Galactic origin or its source being located within a prominent star-forming galaxy. Instead, the source appears to be co-located with a low-luminosity active galactic nucleus or a previously unknown type of extragalactic source. Localization and identification of a host or counterpart has been essential to understanding the origins and physics of other kinds of transient events, including gamma-ray bursts[12,13] and tidal disruption events[14]. However, if other fast radio bursts have similarly faint radio and optical counterparts, our findings imply that direct subarcsecond localizations may be the only way to provide reliable associations.

The repetition of bursts from FRB 121102[9,10] enabled a targeted interferometric localization campaign with the Karl G. Jansky Very Large Array (VLA) in concert with single-dish observations using the 305-m William E. Gordon Telescope at the Arecibo Observatory. We searched for bursts in VLA data with 5-ms sampling using both beam-forming and imaging techniques[15] (see Methods). In over 83 h of VLA observations distributed over six months, we detected nine bursts from FRB 121102 in the 2.5–3.5-GHz band with signal-to-noise ratios ranging from 10 to 150, all at a consistent sky position.

These bursts were initially detected with real-time de-dispersed imaging and confirmed by a beam-formed search (Fig. 1). From these detections, the average J2000 position of the burst source is right ascension $\alpha = 05$ h 31 min 58.70 s, declination $\delta = +33° 08' 52.5''$, with a 1σ uncertainty of about $0.1''$, consistent with the Arecibo localization[9] but with three orders of magnitude better precision. The dispersion measure (DM) for each burst is consistent with the previously reported value[9] of 558.1 ± 3.3 pc cm^{-3}, with comparable uncertainties. Three bursts detected at the VLA (2.5–3.5 GHz) had simultaneous coverage at Arecibo (1.1–1.7 GHz). After accounting for dispersion delay and light travel time, one burst is detected at both telescopes (Extended Data Table 1), but the other two show no emission in the Arecibo band, implying frequency structure at scales of approximately 1 GHz. This finding provides new constraints on the broadband burst spectra, which previously have shown highly variable structure across the Arecibo band[8-10].

Radio images at 3 GHz produced by integrating the VLA fast-sampled data reveal a continuum source within $0.1''$ of the burst position, which we refer to hereafter as the persistent source. A cumulative 3-GHz image (root-mean-square (r.m.s.) of $\sigma \approx 2\mu$Jy per beam; Fig. 2) shows 68 other sources within a $5'$ radius, with a median flux density of 26μJy. Given the agreement between the positions of the detected bursts and the continuum counterpart, we estimate a probability of chance coincidence of less than 10^{-5}. The persistent source is detected in follow-up VLA observations over the entire frequency range from 1 GHz to 26 GHz. The radio spectrum is broadly consistent with non-thermal emission, although with deviations from a single power-law spectrum. Imaging at 3 GHz over the campaign shows that the persistent source exhibits around 10% variability on day timescales (Fig. 2, Extended Data Table 2). Variability in faint radio sources is common[6,7]; of the 69 sources within a $5'$ radius, nine (including the persistent counterpart) were apparently variable (see Methods). There is no correlation between VLA detections of bursts from FRB 121102 and the flux density of the counterpart at that epoch (Fig. 2, Methods).

Observations with the European Very Long Baseline Interferometry (VLBI) Network and the Very Long Baseline Array detect the persistent source and limit its size to less than 1.7 milliarcseconds (see Methods). The lower limit on the brightness temperature is 8×10^6 K. The source has an integrated flux density that is consistent with that inferred at lower resolution in contemporaneous VLA imaging, indicating the absence of any detectable flux density on spatial scales larger than a few milliarcseconds.

[1]Cornell Center for Astrophysics and Planetary Science and Department of Astronomy, Cornell University, Ithaca, New York 14853, USA. [2]Department of Astronomy and Radio Astronomy Lab, University of California, Berkeley, California 94720, USA. [3]National Radio Astronomy Observatory, Socorro, New Mexico 87801, USA. [4]Department of Physics and Astronomy, West Virginia University, Morgantown, West Virginia 26506, USA. [5]Center for Gravitational Waves and Cosmology, West Virginia University, Chestnut Ridge Research Building, Morgantown, West Virginia 26505, USA. [6]ASTRON, Netherlands Institute for Radio Astronomy, Postbus 2, 7990 AA Dwingeloo, The Netherlands. [7]Anton Pannekoek Institute for Astronomy, University of Amsterdam, Science Park 904, 1098 XH Amsterdam, The Netherlands. [8]Academia Sinica Institute of Astronomy and Astrophysics, 645 North A'ohoku Place, Hilo, Hawaii 96720, USA. [9]Department of Physics and McGill Space Institute, McGill University, 3600 University Street, Montreal, Quebec H3A 2T8, Canada. [10]Arecibo Observatory, HC3 Box 53995, Arecibo, Puerto Rico 00612, USA. [11]National Research Council of Canada, Herzberg Astronomy and Astrophysics, Dominion Radio Astrophysical Observatory, PO Box 248, Penticton, British Columbia V2A 6J9, Canada. [12]Haverford College, 370 Lancaster Avenue, Haverford, Pennsylvania 19041, USA. [13]Columbia Astrophysics Laboratory, Columbia University, New York, New York 10027, USA. [14]Joint Institute for VLBI ERIC, Postbus 2, 7990 AA Dwingeloo, The Netherlands. [15]Jet Propulsion Laboratory, California Institute of Technology, Pasadena, California 91109, USA. [16]National Radio Astronomy Observatory, Charlottesville, Virginia 22903, USA. [17]Max-Planck-Institut für Radioastronomie, Auf dem Hügel 69, Bonn D-53121, Germany. [18]Sterrewacht Leiden, Leiden University, Postbus 9513, 2300 RA Leiden, The Netherlands.
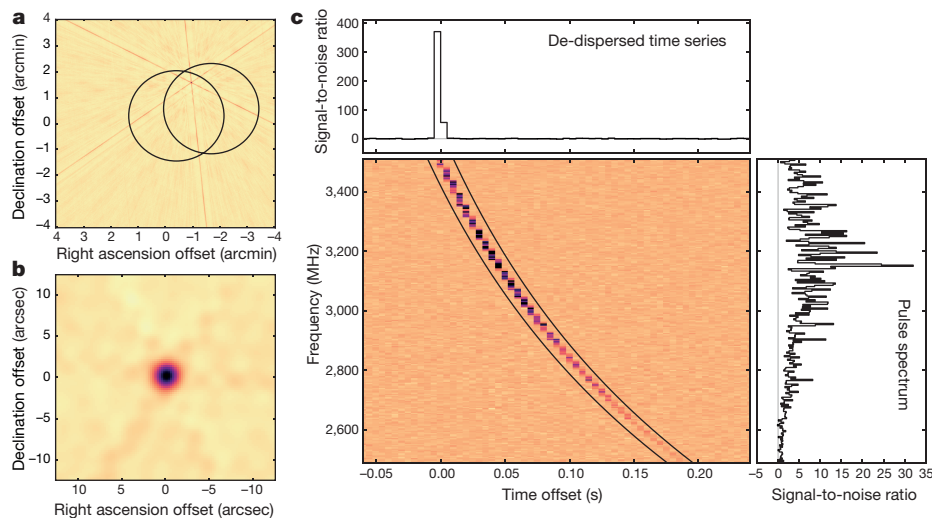
Figure 1 | VLA detection of FRB 121102. a, A 5-ms dispersion-corrected dirty image showing a burst from FRB 121102 at MJD 57633.67986367 (2016 September 2). The approximate localization uncertainty from previous Arecibo detections[9] ($3'$ beam full-width at half-maximum (FWHM)) is shown with overlapping circles. **b**, A zoomed-in portion of **a**, deconvolved and re-centred on the detection, showing the approximately $0.1''$ localization of the burst. **c**, Time–frequency data extracted from phased VLA visibilities at the burst location shows the ν^{-2} dispersive sweep of the burst. The solid black lines illustrate the expected sweep for $DM = 558$ pc cm^{-3}. The de-dispersed lightcurve and spectra are projected to the upper and right panels, respectively. In all panels, the colour scale indicates the flux density.

We have searched for counterparts at submillimetre, infrared, optical and X-ray wavelengths using archival data and a series of new observations. A coincident unresolved optical source is detected in archival 2014 Keck data (R-band AB magnitude of 24.9 ± 0.1) and in recently obtained Gemini data (r-band AB magnitude of 25.1 ± 0.1; Fig. 2), with a chance coincidence probability of less than 3.5×10^{-4} (see Methods). The source is undetected in archival infrared observations, in ALMA 230-GHz observations, and in XMM-Newton and Chandra X-ray imaging (see Methods). The spectral energy distribution of the persistent source is compared in Fig. 3 to some example spectra for known source types, none of which matches our observations well.

The observations reported here corroborate the strong arguments[10] against a Galactic location for the source. As argued previously, stellar radio flares can exhibit swept-frequency radio bursts on subsecond timescales[16], but they do not strictly adhere to the ν^{-2} dispersion law (where ν is the frequency) seen for FRB 121102[9,10], nor are they expected to show constant apparent DM. The source of the sizable DM excess—three times the Galactic maximum predicted by the NE2001 electron-density model[17]—is not revealed as a H II region, a supernova remnant or a pulsar-wind nebula in our Galaxy, which would appear extended at radio, infrared or Hα[10] wavelengths at our localized position. Spitzer mid-infrared limits constrain substellar objects with temperatures of more than 900 K to be at distances of 70 pc or greater, and the Gemini detection sets a minimum distance of about 1 kpc and 100 kpc for stars with effective temperatures greater than 3,000 K and 5,000 K, respectively. These limits rule out Galactic stars that could plausibly account for the DM excess and produce the radio continuum counterpart. We conclude that FRB 121102 and its persistent counterpart do not correspond to any known class of Galactic source.
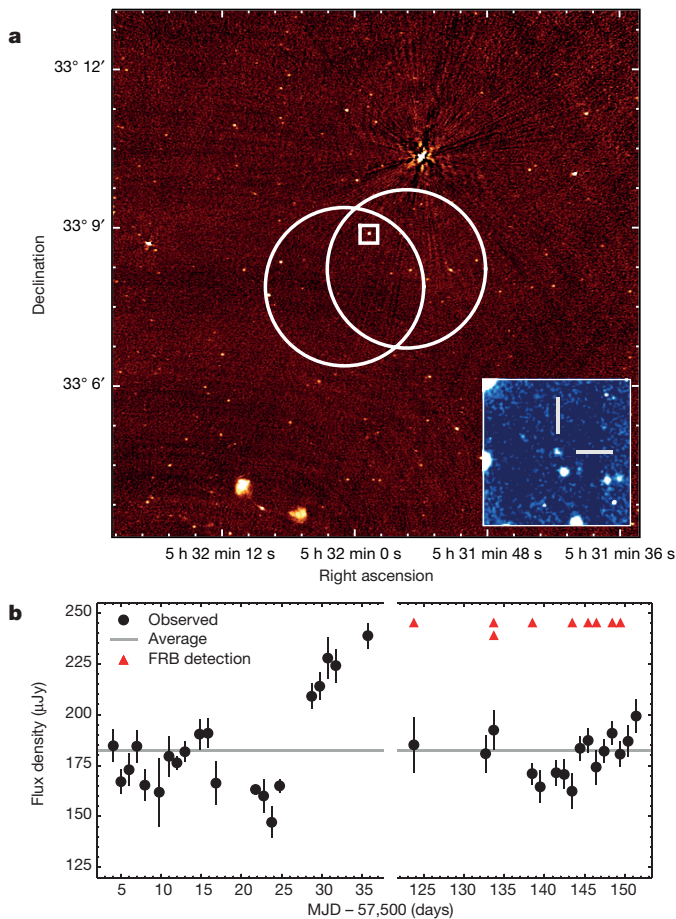
The simplest interpretation is that the burst source resides in a host galaxy that also contains the persistent radio counterpart. If so, the DM of the burst source has contributions from the electron density in the Milky Way disk (DM$_{NE2001}$) and halo (DM$_{halo}$)[17], the intergalactic medium (DM$_{IGM}$)[18] and the host galaxy (DM$_{host}$); we estimate DM$_{IGM}$ = DM − DM$_{NE2001}$ − DM$_{halo}$ − DM$_{host}$ ≈ 340 pc cm^{-3} − DM$_{host}$, with DM$_{NE2001}$ = 188 pc cm^{-3} and DM$_{halo}$ ≈ 30 pc cm^{-3}. The maximum redshift of the fast radio burst, for DM$_{host}$ = 0, is $z_{FRB} \approx 0.32$, which corresponds to a maximum luminosity distance of 1.7 Gpc. Variance in the mapping of DM to redshift[19] ($\sigma_z = \sigma_{DM}(dz/dDM) \approx 0.1$) could increase the upper bound to $z \approx 0.42$. Alternatively, a sizable host-galaxy

contribution could imply a low redshift and a negligible contribution from the intergalactic medium, although no such galaxy is apparent. Hereafter we adopt $z_{FRB} \lesssim 0.32$.

The faint optical detection and the non-detection at 230 GHz with ALMA imply a low star-formation rate within any host galaxy. For our ALMA 3σ upper limit of 51 μJy and a submillimetre spectral index of 4, we estimate the star-formation rate[20] to be less than $(0.06–19)M_\odot$ yr^{-1} (where $M_\odot$ is the mass of the Sun) for redshifts z ranging from 0.01 to 0.32 (luminosity distances of 43 Mpc to 1.7 Gpc), respectively. The implied absolute magnitude of approximately −16 at $z = 0.32$ is similar to that of the Small Magellanic Cloud, whose mass of around $10^9 M_\odot$ would correspond to an upper limit on the mass of the host galaxy.

The compactness of the persistent radio source (less than about 8 pc for $z \lesssim 0.32$) implies that it does not correspond to emission from an extended galaxy or a star-forming region[21], although our brightness temperature limits do not require the emission to be coherent. Its size and spectrum appear consistent with a low-luminosity active galactic nucleus (AGN), but X-ray limits do not support this interpretation. Young extragalactic supernova remnants[22] can have brightness temperatures in excess of 10^7 K, but they typically have simple power-law spectra and exhibit stronger variability.

The burst source and persistent source have a projected separation of less than about 500 pc assuming $z \lesssim 0.32$. There are three broad interpretations of their relationship. First, they may be unrelated objects harboured in a host galaxy, such as a neutron star (or other compact object) and an AGN. Alternatively, the two objects may interact, for example, producing repeated bursts from a neutron star very close to an AGN[3,23,24]. A third possibility is that they are a single source. This possibility could involve unprecedented bursts from an AGN[25] along with persistent synchrotron radiation; or persistent emission might comprise high-rate bursts too weak to detect individually, with bright detectable bursts forming a long tail of the amplitude distribution. In this interpretation, the difficulty in establishing any periodicity in the observed bursts[9,10] may result from irregular beaming from a rotating compact object or extreme spin or orbital dynamics. The Crab pulsar and some millisecond pulsars display bimodality[26,27] in giant and regular pulses. However, they show well-defined periodicities and have steep spectra that are inconsistent with the spectrum of the persistent source, which extends to at least 25 GHz. Magnetars show broad spectra that extend beyond 100 GHz in a few cases, but differ from the roll-off of the spectrum of the persistent source.
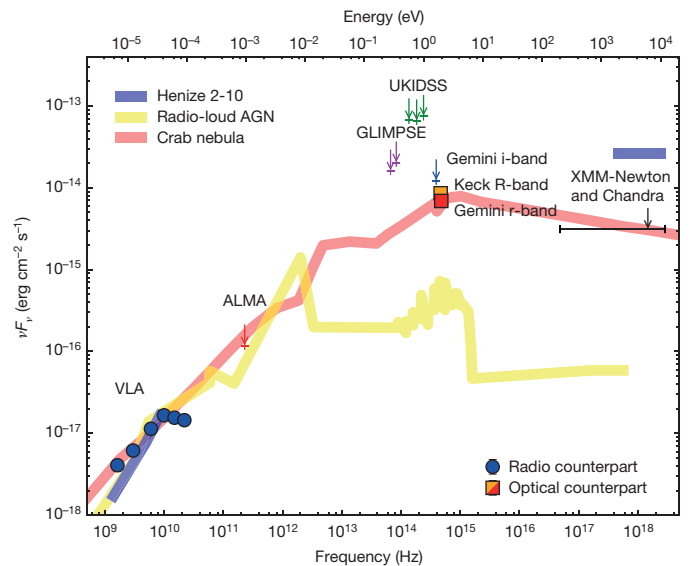
a

b

Figure 3 | Broadband spectral energy distribution of the counterpart.
Detections of the persistent radio source (blue circles), the optical
counterpart (red and orange squares) and 5σ upper limits at various
frequency bands (arrows) are shown; see Methods for details. Spectral
energy distributions of other radio point sources are scaled to match the
radio flux density at 10 GHz and overlaid for comparison: low-luminosity
AGN in Henize 2-10, a star-forming dwarf galaxy[28] placed at 25 Mpc
(blue); radio-loud AGN QSO 2128−123[29] scaled by $10^{-4.3}$ to simulate a
lower-luminosity AGN and placed at 3 Gpc (yellow); and the Crab nebula[30]
at 4 Mpc (red). F_ν is the flux density and νF_ν is the flux density weighted by
photon energy.

Figure 2 | Radio and optical images of the FRB 121102 field. a, VLA
image at 3 GHz with a combination of array configurations. The image
resolution is $2''$ and the r.m.s. is $\sigma = 2\,\mu$Jy per beam. The Arecibo detection[9]
uncertainty regions ($3'$ beam FWHM) are indicated with overlapping
white circles. The radio counterpart of the bursts detected at the VLA is
highlighted by a $20''$ white square within the overlap region. The colour
scale indicates the observed flux density. Inset, Gemini r-band image of
the $20''$ square shows an optical counterpart ($r_{AB} = 25.1 \pm 0.1$ mag), as
identified by the $5''$ bars. **b**, The light curve of the persistent radio source
coincident with FRB 121102 over the course of the VLA campaign,
indicating variability on timescales shorter than 1 day. Error bars are 1σ.
The average flux density of the source of about $180\,\mu$Jy is marked in grey,
and the epochs at which bursts were detected at the VLA are indicated
(red triangles). The variability of the persistent radio counterpart is
uncorrelated with the detection of bursts (see Methods).

All things considered, we cannot favour any one of these interpre-
tations. Future comparison of spectra from the persistent source and
from individual bursts could rule out the 'single source' interpreta-
tion. The proximity of the two sources and their physical relationship
can be probed by detecting a burst in VLBI observations or by using
interstellar scintillations, which can resolve separations of less than
one milliarcsecond.

If other fast radio bursts are similar to FRB 121102, then our dis-
covery implies that direct subarcsecond localizations of bursts are so
far the only secure way to find associations. The unremarkable nature
of the counterparts to FRB 121102 suggests that efforts to identify the
counterparts of other fast radio bursts in large error boxes will be dif-
ficult and, given the lack of correlation between the variability of the
persistent source and the bursts, rapid post-fast-radio-burst follow-up
imaging in general may not be fruitful.

Online Content Methods, along with any additional Extended Data display items and
Source Data, are available in the online version of the paper; references unique to
these sections appear only in the online paper.

1. Lorimer, D. R., Bailes, M., McLaughlin, M. A., Narkevic, D. J. & Crawford, F.
   A bright millisecond radio burst of extragalactic origin. *Science* **318,** 777–780
   (2007).
2. Thornton, D. *et al.* A population of fast radio bursts at cosmological distances.
   Science **341,** 53–56 (2013).
3. Cordes, J. M. & Wasserman, I. Supergiant pulses from extragalactic neutron
   stars. *Mon. Not. R. Astron. Soc.* **457,** 232–257 (2016).
4. Keane, E. F. *et al.* The host galaxy of a fast radio burst. *Nature* **530,** 453–456
   (2016).
5. Loeb, A., Shvartzvald, Y. & Maoz, D. Fast radio bursts may originate from
   nearby flaring stars. *Mon. Not. R. Astron. Soc.* **439,** L46–L50 (2014).
6. Williams, P. K. G. & Berger, E. No precise localization for FRB 150418: claimed
   radio transient is AGN Variability. *Astrophys. J.* **821,** L22 (2016).
7. Vedantham, H. K. *et al.* On associating fast radio bursts with afterglows.
   Astrophys. J. **824,** L9 (2016).
8. Spitler, L. G. *et al.* Fast radio burst discovered in the Arecibo pulsar ALFA
   survey. *Astrophys. J.* **790,** 101 (2014).
9. Spitler, L. G. *et al.* A repeating fast radio burst. *Nature* **531,** 202–205 (2016).
10. Scholz, P. *et al.* The repeating fast radio burst FRB 121102: multi-wavelength
    observations and additional bursts. *Astrophys. J.* (in the press); preprint at
    https://arxiv.org/abs/1603.08880.
11. Petroff, E. *et al.* A survey of FRB fields: limits on repeatability. *Mon. Not. R.
    Astron. Soc.* **454,** 457–462 (2015).
12. Metzger, M. R. *et al.* Spectral constraints on the redshift of the optical
    counterpart to the γ-ray burst of 8 May 1997. *Nature* **387,** 878–880 (1997).
13. Bloom, J. S., Kulkarni, S. R. & Djorgovski, S. G. The observed offset distribution
    of gamma-ray bursts from their host galaxies: a robust clue to the nature of
    the progenitors. *Astron. J* **123,** 1111–1148 (2002).
14. Gezari, S. *et al.* Ultraviolet detection of the tidal disruption of a star by a
    supermassive black hole. *Astrophys. J.* **653,** L25–L28 (2006).
15. Law, C. J. *et al.* A millisecond interferometric search for fast radio bursts with
    the Very Large Array. *Astrophys. J.* **807,** 16 (2015).
16. Maoz, D. *et al.* Fast radio bursts: the observational case for a Galactic origin.
    Mon. Not. R. Astron. Soc. **454,** 2183–2189 (2015).
17. Cordes, J. M. & Lazio, T. J. W. NE2001.I. A new model for the galactic
    distribution of free electrons and its fluctuations. Preprint at http://arxiv.org/
    abs/astro-ph/0207156 (2002).
18. Inoue, S. Probing the cosmic reionization history and local environment of
    gamma-ray bursts through radio dispersion. *Mon. Not. R. Astron. Soc.* **348,**
    999–1008 (2004).
19. McQuinn, M. Locating the "missing" baryons with extragalactic dispersion
    measure estimates. *Astrophys. J.* **780,** L33 (2014).

20. Carilli, C. L. & Yun, M. S. The radio-to-submillimeter spectral index as a redshift indicator. *Astrophys. J.* **513**, L13–L16 (1999).
21. Condon, J. J. Radio emission from normal galaxies. *Annu. Rev. Astron. Astrophys.* **30**, 575–611 (1992).
22. Lonsdale, C. J., Diamond, P. J., Thrall, H., Smith, H. E. & Lonsdale, C. J. VLBI images of 49 radio supernovae in Arp 220. *Astrophys. J.* **647**, 185–193 (2006).
23. Pen, U.-L. & Connor, L. Local circumnuclear magnetar solution to extragalactic fast radio bursts. *Astrophys. J.* **807**, 179 (2015).
24. Lyubarsky, Y. A model for fast extragalactic radio bursts. *Mon. Not. R. Astron. Soc.* **442**, L9–L13 (2014).
25. Romero, G. E., del Valle, M. V. & Vieyro, F. L. Mechanism for fast radio bursts. *Phys. Rev. D* **93**, 023001 (2016).
26. Lundgren, S. C. *et al.* Giant pulses from the crab pulsar: a joint radio and gamma-ray study. *Astrophys. J.* **453**, 433–445 (1995).
27. Kinkhabwala, A. & Thorsett, S. E. Multifrequency observations of giant radio pulses from the millisecond pulsar B1937+21. *Astrophys. J.* **535**, 365–372 (2000).
28. Reines, A. E. & Deller, A. T. Parsec-scale radio emission from the low-luminosity active galactic nucleus in the dwarf starburst galaxy Henize 2-10. *Astrophys. J.* **750**, L24 (2012).
29. Elvis, M. *et al.* Atlas of quasar energy distributions. *Astrophys. J. Suppl. Ser.* **95**, 1–68 (1994).
30. Bühler, R. & Blandford, R. The surprising Crab pulsar and its nebula: a review. *Rep. Prog. Phys.* **77**, 066901 (2014).

Supplementary Information is available in the online version of the paper.

Author Contributions S.C. was principal investigator of the localization campaign described here. C.J.L. and S.B.-S. are principal investigators of the realfast project and performed the analysis that achieved the first VLA burst detections. S.C., C.J.L., R.S.W., S.B.-S., G.C.B., B.B. and P.D. performed detailed analysis of the VLA data. S.B.-S. and B.B. led the analysis of the VLA multi-band spectral data. J.W.T.H. was principal investigator of the EVN observations, which were analysed by Z.P. and B.M. G.C.B. was principal investigator of the VLBA observations, and led their analysis. J.W.T.H., A.S. and L.G.S. led the execution and analysis of the parallel Arecibo observing campaign. P.D. led the commissioning of fast-sampled VLA observing modes. S.C. was principal investigator of the ALMA observations. P.S. was principal investigator of the X-ray observations, and performed the X-ray analysis, along with S.B. S.P.T. was principal investigator of the Gemini observations, and along with C.G.B. led the analysis of Keck, Gemini and archival UKIDSS and GLIMPSE data. S.C. and C.J.L. led the writing of the manuscript, with substantial contributions from J.M.C. and J.W.T.H. All authors contributed substantially to the interpretation of the analysis results and to the final version of the manuscript.

METHODS

Observation strategy. Detection and precise localization of a fast radio burst requires approximately arcsecond angular resolution, millisecond time resolution and megahertz frequency resolution. In 2015 November, we conducted 10 h of fast-dump (5 ms) observations of the FRB 121102 field with the VLA[10] at 1.6 GHz, with no burst detections. In 2016 April–May, we observed for 40 h at 3 GHz and again detected no bursts with either our fast-imaging or beam-forming pipeline (described below). Detections of FRB 121102 with the 305-m Arecibo telescope[9,10] suggested that VLA detections might be sensitivity limited, leading us to conduct a simultaneous observing campaign where Arecibo would identify a burst in the time domain and contemporaneous VLA observations would precisely localize it. In practice, this proved to be unnecessary for VLA detection, but it provided a wider frequency band to characterize the burst spectra.

Arecibo observations. Arecibo observations used the L-wide receiver, which provides a frequency range of 1.15−1.73 GHz. The PUPPI pulsar backend recorded full Stokes polarization information, with time and frequency resolutions of 10.24 μs and 1.5625 MHz, respectively. Each frequency channel was coherently de-dispersed to 557 pc cm^{-3}, thereby eliminating intra-channel dispersion smearing.

VLA fast-dump observations. The VLA fast-sampled interferometric data were recorded with 5-ms integration time, 256 channels and a bandwidth of 1,024 MHz centred at 3 GHz. We first detected FRB 121102 on 2016 August 23 with a signal-to-noise ratio of about 35. Until 2016 September, we continued coordinated Arecibo and VLA observations, detecting another eight bursts at the same location and DM. In total, we acquired about 83 h of fast-dump interferometric observations in three sessions: 2015 November[10] at 1.6 GHz, 2016 April–May at 3 GHz, and 2016 August–September at 3 GHz with some observing at 6 GHz.

Millisecond imaging with fast-dump visibility data. During the coordinated campaign, all of the bursts were detected with real-time analysis within hours of the data being recorded by the realfast[15] system at the VLA. The real-time processing system de-dispersed visibilities to a small range of values centred on DM = 557.0 pc cm^{-3}. For each integration and DM value, the pipeline formed a Stokes I image on timescales from 5 ms to 80 ms and saved images with peak signal-to-noise ratios greater than 7.4—a threshold based on the known false-positive rate due to thermal noise.

All candidates were re-analysed offline with improved calibration, data cleaning and refined localization using both custom, Python-based software and CASA. We calibrated and imaged de-dispersed visibilities with a typical sensitivity (1σ) of 5 mJy in 5 ms. Extended Data Table 1 lists burst properties, and the brightest detection is shown in Fig. 1. By fitting a model of the synthesized beam to an image of the burst, we measure burst locations with statistical errors of better than 0.3″. However, the locations are affected by systematic errors at the level of about 1% of the synthesized beam sizes, a modest effect that is evident when comparing the localizations of the first four VLA burst detections (beam sizes of about 2.5″ × 2″) with the last five (beam sizes of about 1.3″ × 0.8″). Using only the last five burst centroids (with lower residual systematics owing to the narrower beam), we find that the burst locations are consistent with the centroid of the persistent radio continuum counterpart (Extended Data Table 3, Extended Data Fig. 1). The location of the radio continuum counterpart is measured from the error-weighted mean of the location measured in deep imaging from 1 GHz to 26 GHz (see below). The error in the offset is calculated from the quadrature sum of errors in each burst and the counterpart.

Beam-forming analysis with fast-dump visibility data. Beam-forming is complementary to millisecond imaging: instead of de-dispersing interferometric visibilities and searching for bursts in the image domain, the visibilities are summed with appropriate phasing to produce time–frequency data that can be searched for dispersed bursts. For the VLA observations, the calibration tables generated from time-averaged data (see below) were applied to the fast-dump visibility data, and custom Python software and existing CASA tools were used to extract time–frequency data per beam from a tiling of synthesized beams covering the source region. The time–frequency data from each beam were then written to PSRFITS format and run through a single pulse search pipeline that used PRESTO pulsar processing tools. Single pulse candidates from all of the synthesized beams were jointly filtered to remove candidates that occurred simultaneously in many beams, as well as candidates that were narrow-band, because these were probably caused by radio-frequency interference. Diagnostic plots for the remaining candidates were examined by eye for bursts. The beam-forming pipeline was used to independently verify the times and positions of each of the VLA-detected bursts. For the example shown in Fig. 1, the instrumental time resolution for the observations (5 ms) is much larger than both the intrinsic pulse width and the intra-channel DM smearing, leading to a pixelated appearance.

VLA imaging observations of the persistent counterpart. The 3-GHz VLA fast-dump observations were also averaged down to lower time resolution, calibrated using the standard VLA pipeline procedures with CASA[32], and imaged at each

epoch. Once the persistent counterpart to FRB 121102 had been identified, we used these per-epoch images to construct the light curve of the source, as well as a deep average image of the sky (Fig. 2, Extended Data Table 2). The variability of the persistent radio counterpart is uncorrelated with the detection of bursts; the point biserial correlation coefficient between the detection (or not) of a burst and the flux density of the counterpart is $r = -0.054$, which would be exceeded by chance about 75% of the time. Of the 69 sources detected within a 5′ radius, 9 (including the persistent counterpart) showed significant variability, as measured by the reduced chi-squared statistic, $\chi_r^2 = 1/(N-1)\sum_t (S_t - \overline{S})^2/\sigma_t^2 > 5.0$, where S_t is the flux density of the source and σ_t is the image r.m.s. at epoch t, and $\overline{S}$ is the epoch-averaged flux density over $N = 22$ epochs.

We also acquired VLA imaging data covering a contiguous frequency range from 1 GHz to 26 GHz. These observations used six separate receivers on the VLA: L- (1–2 GHz); S- (2–4 GHz); C- (4–8 GHz); X- (8–12 GHz); Ku- (12–18 GHz); and K-band (18–26 GHz). Observations were carried out on 2016 September 6 and 9, when the VLA was in the B-configuration, with maximum spacing between antennas of roughly 11 km (on September 9, a few antennas had been moved to their A-configuration locations). A third epoch was observed on September 28, at only C-band, with the VLA in the most extended A-configuration. Visibilities were dumped every 2 s, with channel widths of either 1 MHz or 2 MHz (depending on band). Calibration of the flux density scale was done using an observation of the quasar 3C 48 at all bands[33], and the secondary calibrator J0555+3948 was used to monitor complex gain (amplitude and phase) fluctuations as a function of time throughout each of the observations. Standard calibration was done with the VLA calibration pipeline, and subsequent imaging done in both CASA and AIPS. Final flux densities were estimated using several techniques to provide a cross-check, including *imfit* in CASA, *JMFIT* in AIPS, summing up CLEAN component flux density and summing up flux density in the image pixels. Positions were measured using *JMFIT*. The two epochs (three for C-band) were imaged separately and results between the two (three) were found to agree to within the uncertainties (Extended Data Fig. 2), so visibility data from the two epochs (three for C-band) were combined together to make the final images. Results are reported in Extended Data Table 3 and the measurements are plotted as part of the broadband spectral energy distribution (Fig. 3).

Very long baseline interferometry with the European VLBI Network. The European VLBI Network (EVN) observed at 1.65 GHz in five epochs (2016 February 2, 10–11, 11–12 and 2016 May 24, 25) for about 2 h per session. The array included the 100-m Effelsberg, the 76-m Jodrell Bank, the 32-m Medicina, the 25-m Onsala, the 32-m Torun, the 25-m Westerbork (single dish) and the 305-m Arecibo telescopes. The data were streamed to the EVN Software Correlator (SFXC) at the Joint Institute for VLBI ERIC (JIVE) in Dwingeloo, at a data rate of 1,024 Mbit s^{-1} (512 Mbit s^{-1} for Arecibo) in real time. The individual station voltages were recorded simultaneously as well. During the first epoch, the ICRF source J0518+3306 was used as a phase-reference calibrator (separation from the field of about 2.9°) and observations were alternated between the field (8 min) and the calibrator (2 min). For subsequent epochs we used J0529+3209 as phase-reference calibrator (separation of about 1.1°) because it was proven to be sufficiently bright (approximately 60 mJy) and compact for the EVN from the first-epoch observations.

Following the VLA localization of FRB 121102, we re-correlated all our observations with the phase centre at the FRB 121102 position. The data were analysed with AIPS following standard procedures, and the images were made with the Caltech *Difmap* package. We did not detect the persistent counterpart during the first epoch owing to a combination of technical failures and the distant phase calibrator. In the subsequent epochs we detected the persistent counterpart as a slightly resolved source with a typical peak brightness of about 100 μJy per beam and integrated flux density of about 200 μJy, and deconvolved source size of about 5 mas × 3 mas at a position angle of 140°. The naturally weighted beam size was about 18 mas × 2.2 mas in all cases, with a major axis position angle of −54°; the noise was 7 μJy per beam. Lower limits on the brightness temperatures from the four successful epochs are 7×10^6 K; see Extended Data Fig. 2 and Extended Data Table 3.

Very long baseline interferometry with the Very Long Baseline Array. The NRAO Very Long Baseline Array (VLBA) observed on 2016 September 9 and 16 with 8-h tracks per epoch. First-epoch observations were at 1.392–1.680 GHz, with a synthesized beam size of 11.3 mas × 5.0 mas at a position angle of 163.7°. Second-epoch observations were at 4.852–5.076 GHz (beam size of 2.74 mas × 1.43 mas at a position angle of 174.8°). A total recording bandwidth of 2 Gbits s^{-1} with dual circular polarizations was obtained for each observation. As in the EVN observations, the compact calibrator J0529+3209 was used to provide phase-referencing solutions for FRB 121102. Standard interferometric calibrations were applied using AIPS. Images of the field achieved 17 μJy per beam and 12 μJy per beam r.m.s. at 1.5 GHz and 5.0 GHz, respectively. The persistent counterpart to

FRB 121102 was clearly detected in both observations with partially resolved compact structure. At 1.5 GHz, two-dimensional Gaussian deconvolution yields a size of 4.6 mas × 3.3 mas, whereas the 5.0-GHz upper limit on the deconvolved size is <1.73 mas. Lower limits on the brightness temperatures from the two epochs are 8×10^6 K and 3×10^6 K; see Extended Data Fig. 2 and Extended Data Table 3.

Atacama Large Millimeter Array observations. The Atacama Large Millimeter and Submillimeter Array (ALMA) observed on 2016 September 15, using Band 6 and covering 8 GHz of bandwidth in the range 220–240 GHz (with 2-MHz channels). We used 38 antennas in the C40-6 configuration, yielding a resolution of $0.32'' \times 0.13''$. Calibration and imaging was provided by the ALMA observatory and done using CASA via the ALMA pipeline. The image r.m.s. noise level was 17 μJy per beam and did not reveal any significant (>5σ) sources.

Optical and infrared imaging. We used the following optical imaging data: 630-s Keck R-band image from 2014 November 19, 120-s Gemini i-band image (2016 March 17) and 1250-s Gemini r-band image (2016 October 24, 25). The data were reduced with a combination of IRAF, IDL and Python tools. We used the URAT1 catalogue[34] as an astrometric reference frame. The astrometric errors were <80–90 mas (r.m.s.) in all frames. We used the IPHAS photometry[35] to measure the zero-point correction for the co-added images. A counterpart to FRB 121102 is detected in the archival Keck image at $R_{AB} = 24.9 \pm 0.1$ mag and in the Gemini GMOS r-band image at $r_{AB} = 25.1 \pm 0.1$ mag, consistent with being point-like in $0.7''$ seeing. A non-detection in the i-band image yields an upper limit of $i > 24$. The r-band centroid position was measured to be $\alpha = 05\,h\,31\,min\,58.69\,s$, $\delta = +33° 08' 52.51''$ (J2000) with an astrometric error of approximately 100 mas, consistent with the R-band position. We measure a stellar density of 1.12×10^{-2} arcsec^{-2} for $r_{AB} < 25.1$. Therefore, the chance coincidence probability of finding the optical counterpart within a 100-mas radius of the radio position is $<3.5 \times 10^{-4}$. In regions around the FRB 121102, we derive an upper limit of $r = 26.2$ AB mag arcsec^{-2} (5σ) for any diffuse emission from an extended galaxy, ruling out most of the massive ultralow-surface-brightness galaxies[36]. These galaxies are as large as the Milky Way and would have been more than $5''$ in diameter if placed at a redshift of $z_{DM} = 0.3$. Smoothing the image with a $5''$ FWHM Gaussian kernel reveals no significant emission (>5σ) on those scales.

The counterpart is not detected in near- and mid-infrared observations from the UKIDSS[37] and Deep GLIMPSE[38,39] surveys with upper limits of $J = 19.8$, $H = 19.0$ and $K = 18.0$ for UKIDSS and 17.8 and 17.3 for the GLIMPSE 3.6-μm and 4.5-μm bands. At the location of FRB 121102, the total V-band absorption, as determined from the COBE/DIRBE dust maps[40], is 2.42 mag. We use published extinction coefficients[41] to correct for absorption in the other bands. Published zero-points and effective wavelengths[42–44] and the IRAC Instrument Handbook v2.1.2 were used to obtain the flux density measurements and limits shown in the broadband spectrum of the persistent counterpart (Fig. 3).

X-ray imaging with XMM-Newton and the Chandra X-ray Observatory. X-ray observations were done with XMM-Newton (IDs 0790180201, 0790180501, 0792382801 and 0792382901) and the Chandra X-ray Observatory (ID 18717). The cameras on-board XMM-Newton consist of one EPIC-pn[45] and two EPIC-MOS[46] CCD arrays. The Chandra observation used the ACIS-S3 detector in TE mode. Two XMM-Newton observations occurred in 2016 February–March, before we achieved our precise localization, with pn in 'large window' mode and the MOS cameras in 'full frame' mode. Two more observations were performed in 2016 September with the pn camera in 'small window' mode and the MOS cameras in 'timing' mode. A 40-ks Chandra observation was performed in 2015 November. In the first two XMM-Newton observations, the pn data were not usable for imaging FRB 121102 because it was positioned at the edge of a CCD chip. The MOS timing-mode observations are also not usable for imaging purposes. We therefore used 41 ks of pn data from 2016 September and 60 ks of MOS data from 2016 February–March for X-ray imaging.

We used standard tools from the XMM Science Analysis System (SAS) version 14.0, HEASoft version 6.19 and CAIO version 4.7 to reduce the data. The XMM-Newton images were mosaicked together using *emosaic* using exposure maps from *eexpmap*. The number of counts in a circular region of radius $18''$ and $1''$ for XMM-Newton and Chandra, respectively, centred at the position of FRB 121102 were compared to several randomly selected background regions. No significant deviation from the background was found; the 5σ count-rate limits are $<3 \times 10^{-4}$ counts s^{-1} and $<2 \times 10^{-4}$ counts s^{-1}. To place a flux limit we assume a photoelectrically absorbed power-law spectrum with a spectral index of $\Gamma = 2$ and a hydrogen column density of $N_H = 1.7 \times 10^{22}$ cm^{-2} (implied by its relation with DM[47]). Taking into account the energy-dependent effective area and Poisson statistics of the telescopes, we place a 5σ limit of 5×10^{-15} erg s^{-1} cm^{-2} at 0.5–10 keV on an X-ray point source at the location of FRB 121102 using the mosaicked XMM-Newton image. Using the same procedure on the Chandra image also results in a limit of 5×10^{-15} erg s^{-1} cm^{-2} at 0.5–10 keV.

Observational constraints on FRB 121102 and its persistent counterpart. Our observations support the conclusion that no Galactic source can explain the observed DM excess. If the compact counterpart contributes the excess DM over the maximum predicted by NE2001 along this line of sight, then the requirement that it be optically thin[10] at 1.4 GHz implies a lower limit on its size ($L > 0.03$ pc) and, hence, the source distance. The VLBA and EVN compactness limits (<1.7 mas in any case, ignoring scattering contributions to angular extent) imply a minimum distance of 3.6 Mpc, far beyond our Galaxy. The absence of X-ray detections constrains an AGN counterpart. The fundamental plane relation[48] between radio and X-ray luminosities and the black-hole mass predicts that X-ray emission should be detected for black-hole systems with $z < 0.32$ and mass $M_{BH} < 10^9 M_\odot$. However, not all AGN follow this relationship, including radio-loud AGN and systems with jet–interstellar medium interactions. Radio-loud AGN are probably excluded on the basis of the low radio luminosity $L_R \approx 3 \times 10^{41}$ erg s^{-1} at $z = 0.32$. A $10^6 M_\odot$ black hole, which is plausible given the approximately $10^9 M_\odot$ upper limit on the stellar mass, would have to accrete at $<10^{-2}$ below the Eddington rate to match the X-ray upper limit. Our observations are also inconsistent with a young radio supernova remnant, which is typically variable on a timescale of months and associated with star formation[22].

For a nominal gigaparsec-scale distance D corresponding to redshifts $z \lesssim 0.3$, the received fluence A_ν from each burst at a frequency ν over a bandwidth $\Delta\nu$ implies a burst energy of

$$E_{burst} = 4\pi D^2 \frac{\delta\Omega}{4\pi} A_\nu \Delta\nu \approx 10^{38} \text{ erg } \frac{\delta\Omega}{4\pi} D_{Gpc}^2 \frac{A_\nu}{0.1 \text{ Jy ms}} \Delta\nu_{GHz}$$

The unknown solid angle $\delta\Omega$ of the emission could be very small owing to relativistic beaming and, together with a distance possibly much smaller than 1 Gpc, could substantially reduce the energy requirement. However, the total energy emitted could be larger depending on the duration of the emission in the source frame and other model-dependent details. Either way, the burst energies from FRB 121102 are not inconsistent with those that might be expected from the magnetosphere of a compact object[3].

Data availability. All relevant data are available from the corresponding author on reasonable request. VLA visibility data selected for times centred on each of the nine bursts (including Fig. 1) are available at https://dx.doi.org/10.7910/DVN/TLDKXG. Data presented in Figs 2c and 3 and Extended Data Figs 1 and 2 are available as Source Data. The observational data presented here are available from public archives under the following project codes. VLA fast-dump observations: 15B-378, 16A-459, 16A-496; VLA imaging: 16B-385; ALMA: ADS/JAO.ALMA#2015.A.00025.S (http://almascience.org/aq?project_code=2015.A.00025.S); VLBA: 16B-389, 16B-406; EVN: RP024; Gemini: GN-2016A-FT-5, GN-2016B-DD-2.

Code availability. Computational notebooks for reproducing the burst position analysis are available at https://github.com/caseyjlaw/FRB121102. The code used to analyse the data and observations reported here is available at the following sites: realfast (http://realfast.io), RTPipe (https://github.com/caseyjlaw/rtpipe), SDMPy (https://github.com/demorest/sdmpy).

Other standard data reduction packages (AIPS, CASA, Difmap, PyRAF, XMM SAS, HEASoft, CIAO, PRESTO) are available at their respective websites.

32. McMullin, J. P., Waters, B., Schiebel, D., Young, W. & Golap, K. CASA Architecture and Applications. In *Astronomical Data Analysis Software and Systems XVI* (eds Shaw, R. A. *et al.*) 127–130 (ASP Conf. Ser. Vol. 376, Astronomical Society of the Pacific, 2007).

33. Perley, R. A. & Butler, B. J. An accurate flux density scale from 1 to 50 GHz. *Astrophys. J. Suppl. Ser.* **204,** 19 (2013).

34. Zacharias, N. *et al.* The U.S. Naval Observatory Robotic Astrometric Telescope 1st Catalog (URAT1). In *American Astronomical Society Meeting Abstracts* Vol. 225, abstr. 433.01 (American Astronomical Society, 2015).

35. Drew, J. E. *et al.* The INT Photometric Hα Survey of the Northern Galactic Plane (IPHAS). *Mon. Not. R. Astron. Soc.* **362,** 753–776 (2005).

36. van Dokkum, P. G. *et al.* Forty-seven Milky Way-sized, extremely diffuse galaxies in the Coma cluster. *Astrophys. J.* **798,** L45 (2015).

37. Lawrence, A. *et al.* The UKIRT Infrared Deep Sky Survey (UKIDSS). *Mon. Not. R. Astron. Soc.* **379,** 1599–1617 (2007).

38. Benjamin, R. A. *et al.* GLIMPSE. I. An *SIRTF* Legacy project to map the inner galaxy. *Publ. Astron. Soc. Pac.* **115,** 953–964 (2003).

39. Churchwell, E. *et al.* The *Spitzer*/GLIMPSE surveys: a new view of the Milky Way. *Publ. Astron. Soc. Pac.* **121,** 213–230 (2009).

40. Schlegel, D. J., Finkbeiner, D. P. & Davis, M. Maps of dust infrared emission for use in estimation of reddening and cosmic microwave background radiation foregrounds. *Astrophys. J.* **500,** 525–553 (1998).

41. Schlafly, E. F. & Finkbeiner, D. P. Measuring reddening with Sloan Digital Sky Survey stellar spectra and recalibrating SFD. *Astrophys. J.* **737,** 103 (2011).

42. Bessell, M. S., Castelli, F. & Plez, B. Model atmospheres broad-band colors, bolometric corrections and temperature calibrations for O - M stars. *Astron. Astrophys.* **333,** 231–250 (1998).

43. Fukugita, M. *et al.* The Sloan Digital Sky Survey photometric system. *Astron. J.* **111,** 1748–1756 (1996).

44. Hewett, P. C., Warren, S. J., Leggett, S. K. & Hodgkin, S. T. The UKIRT Infrared Deep Sky Survey *ZY JHK* photometric system: passbands and synthetic colours. *Mon. Not. R. Astron. Soc.* **367,** 454–468 (2006).

45. Strüder, L. *et al.* The European Photon Imaging Camera on XMM-Newton: the pn-CCD camera. *Astron. Astrophys.* **365,** L18–L26 (2001).

46. Turner, M. J. L. *et al.* The European Photon Imaging Camera on XMM-Newton: the MOS cameras. *Astron. Astrophys.* **365,** L27–L35 (2001).

47. He, C., Ng, C.-Y. & Kaspi, V. M. The correlation between dispersion measure and X-Ray column density from radio pulsars. *Astrophys. J.* **768,** 64 (2013).

48. Körding, E., Falcke, H. & Corbel, S. Refining the fundamental plane of accreting black holes. *Astron. Astrophys.* **456,** 439–450 (2006).
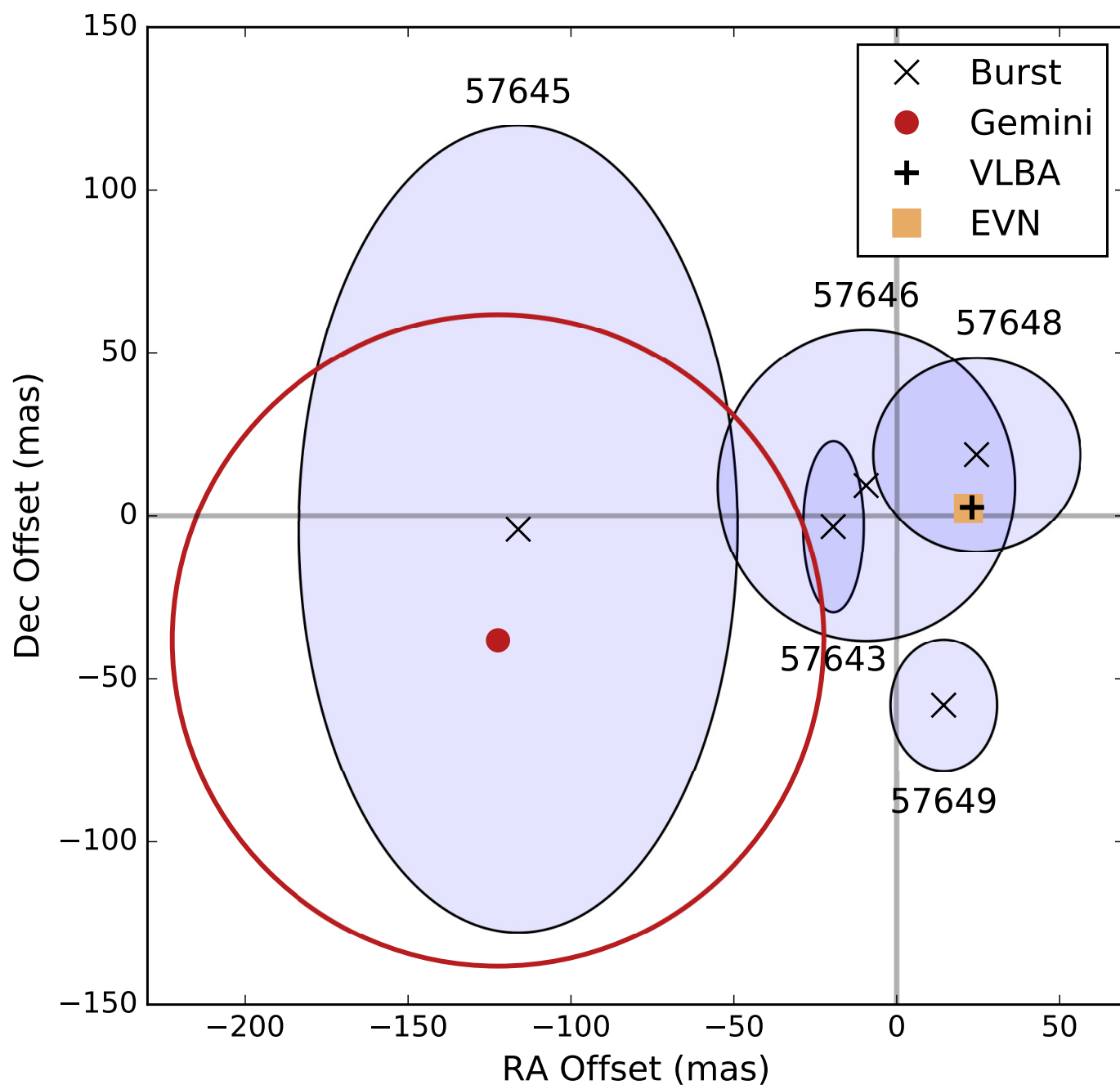
Extended Data Figure 1 | The offset of FRB 121102 from the persistent counterpart. Five bursts detected at the VLA with the highest resolution (A-array, 3 GHz) are plotted (crosses), with epoch indicated by MJD values. The (right ascension (RA), declination (Dec)) coordinate difference (burst relative to counterpart) is shown with an ellipse indicating the 1σ error calculated as the quadrature sum of errors in the two sources. VLBA and EVN positions are indicated, with 1σ errors smaller than the symbols. The centroid of the Gemini optical counterpart is shown (red dot) with an estimated 1σ error circle of 100 mas (red) from fitting and radio-optical frame tie uncertainties.
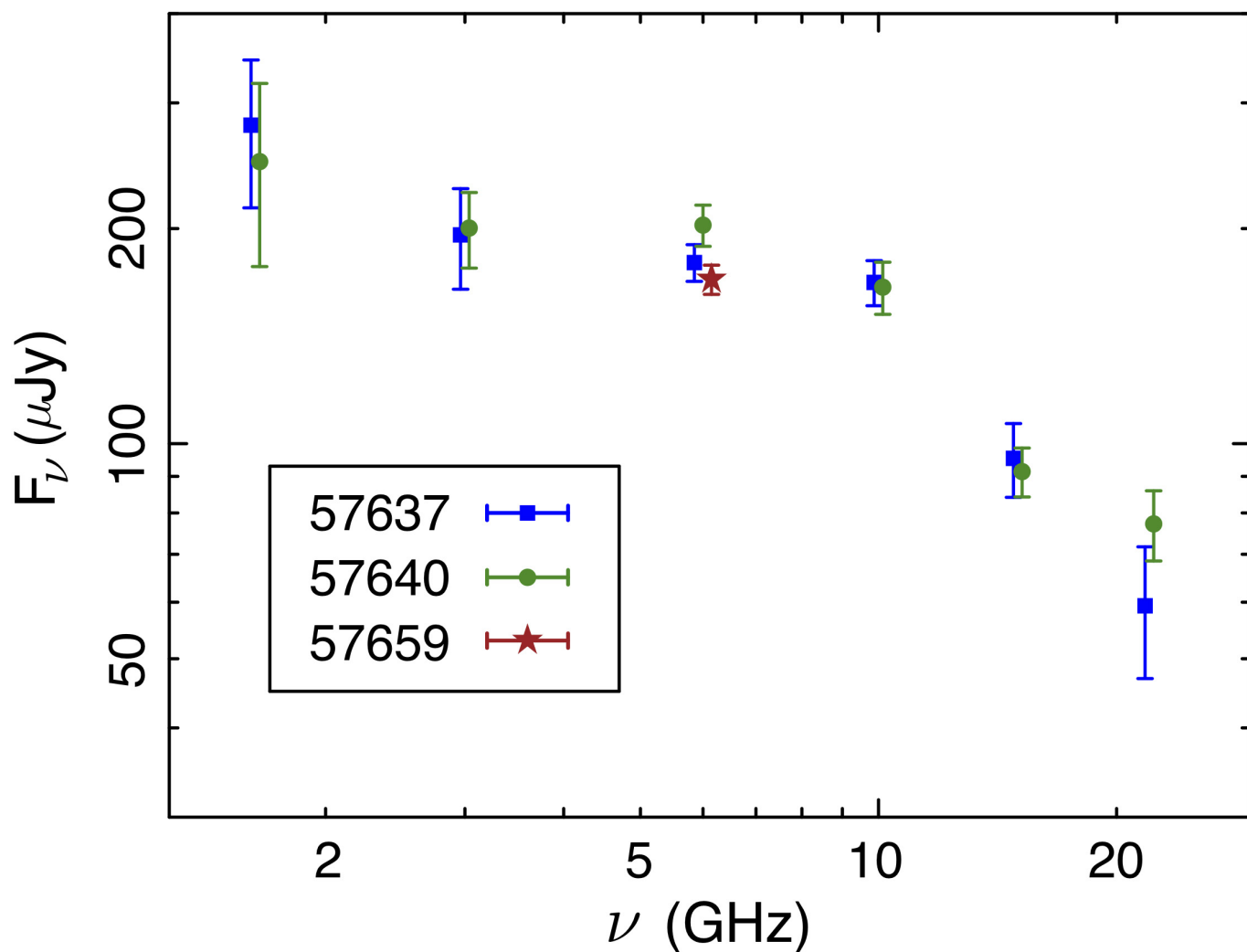
Extended Data Figure 2 | VLA spectrum of the persistent counterpart to FRB 121102. The integrated flux density F_ν is plotted for each epoch of observation (listed by MJD) over a frequency range ν from 1 GHz to 25 GHz. Error bars represent 1σ uncertainties. The spectrum is non-thermal and inconsistent with a single power law.

Extended Data Table 1 | VLA detections of bursts from FRB 121102 and Arecibo constraints

Date	ΔMJD from 57620.0	ΔRA (s)	RA error ('')	ΔDec ('')	Dec error ('')	Beam size ('', '')	S/N ratio	VLA flux density (mJy)	AO flux density (mJy)
23 Aug	3.74402686	0.68	0.05	0.65	0.07	2.8 × 2.3	27[†]	120	–
02 Sep	13.67986367	0.70	0.01	0.48	0.01	2.5 × 2.3	149	670	–
02 Sep	13.69515938	0.70	0.3	0.3	0.3	2.6 × 2.3	7[†]	25	–
07 Sep	18.49937435	0.71	0.07	0.50	0.07	1.9 × 1.7	13	63	–
12 Sep	23.45730263	0.70	0.01	0.55	0.03	1.9 × 0.9	66	326	–
14 Sep	25.42958602	0.69	0.07	0.54	0.12	1.3 × 0.7	10	39	$\lesssim$6
15 Sep	26.46600650	0.70	0.05	0.56	0.05	1.2 × 0.7	10[†]	50	–
17 Sep	28.43691490	0.70	0.03	0.57	0.03	1.3 × 0.8	18	86	~14
18 Sep	29.45175697	0.70	0.02	0.49	0.02	1.3 × 0.8	34	159	$\lesssim$6

Dates are all in the year 2016. Position offsets ΔRA and ΔDec are measured from RA = 05 h 31 min 58 s, Dec = +33° 08′ 52″ (J2000). Topocentric burst MJDs are reported as offsets from MJD 57,620 and are de-dispersed to the top of the VLA band at 3.5 GHz. The flux densities and signal-to-noise (S/N) ratios are estimated from a 5-ms visibility integration, leading to an underestimate because the burst durations are typically shorter in Arecibo detections. Instantaneous beam sizes are listed. Bursts with simultaneous coverage at Arecibo Observatory (AO) at 1.4 GHz are indicated with estimated detection peak flux density in a 5-ms integration, or 5σ upper limits for non-detections. Absence of simultaneous coverage at Arecibo is indicated by dashes.
[†]The real-time analysis of events on 23 August, 2 September and 15 September resulted in detections with signal-to-noise ratios of 35, 16 and 16, respectively. These differences are due to different calibration and flagging approaches between the real-time and offline analyses. The real-time analysis does not include flux-density scale calibration, so the offline analysis gives the best estimate of their flux density.

Extended Data Table 2 | VLA 3-GHz observations of the persistent counterpart to FRB 121102 over time

Date (in 2016)	MJD	Beam size (″, ″)	Flux density (μJy)	Bursts detected
26 Apr	57504.0565	6.25 × 2.42	184.72 ± 7.97	0
27 Apr	57505.0100	6.33 × 1.98	167.08 ± 5.91	0
28 Apr	57506.0181	6.44 × 1.96	172.93 ± 8.01	0
28 Apr	57506.9871	6.14 × 1.98	184.49 ± 7.90	0
29 Apr	57507.9843	6.12 × 1.98	165.37 ± 7.81	0
01 May	57509.7766	8.21 × 1.89	161.90 ± 16.79	0
02 May	57510.9890	6.44 × 2.02	179.54 ± 9.91	0
03 May	57511.9746	6.29 × 2.02	176.34 ± 3.36	0
04 May	57512.9725	6.29 × 1.95	181.78 ± 5.10	0
06 May	57514.7883	7.12 × 1.96	190.43 ± 7.43	0
07 May	57515.8362	6.23 × 2.00	190.86 ± 7.13	0
08 May	57516.8335	6.19 × 2.03	166.36 ± 10.72	0
13 May	57521.7640	6.83 × 1.95	163.23 ± 2.23	0
14 May	57522.7649	6.78 × 1.95	160.06 ± 8.22	0
15 May	57523.7658	6.61 × 1.95	147.13 ± 7.77	0
16 May	57524.7550	8.31 × 1.94	165.03 ± 3.23	0
20 May	57528.7452	1.79 × 1.58	209.01 ± 6.14	0
21 May	57529.7440	1.80 × 1.60	213.95 ± 6.65	0
22 May	57530.7439	1.76 × 1.60	227.76 ± 10.13	0
23 May	57531.7441	1.78 × 1.60	224.08 ± 8.14	0
27 May	57535.7339	1.77 × 1.60	238.78 ± 6.18	0
23 Aug	57623.7454	2.12 × 1.68	185.15 ± 13.56	1
01 Sep	57632.6730	2.22 × 1.71	180.82 ± 9.24	0
02 Sep	57633.6800	1.83 × 1.66	192.39 ± 9.69	2
07 Sep	57638.4685	1.90 × 0.61	171.03 ± 5.21	1
08 Sep	57639.4684	2.02 × 0.60	164.53 ± 7.96	0
10 Sep	57641.4579	1.52 × 0.59	171.46 ± 6.28	0
11 Sep	57642.4581	1.55 × 0.59	170.65 ± 7.21	0
12 Sep	57643.4272	1.56 × 0.58	162.40 ± 8.72	1
13 Sep	57644.4332	1.04 × 0.54	183.47 ± 5.96	0
14 Sep	57645.4307	1.01 × 0.49	187.32 ± 5.92	1
15 Sep	57646.4280	0.99 × 0.49	174.24 ± 8.38	1
16 Sep	57647.4245	1.01 × 0.48	182.05 ± 5.87	0
17 Sep	57648.4161	1.03 × 0.49	190.88 ± 5.69	1
18 Sep	57649.4162	1.02 × 0.49	180.58 ± 6.16	1
19 Sep	57650.4058	1.07 × 0.51	186.93 ± 7.69	0
20 Sep	57651.4058	1.02 × 0.49	199.29 ± 8.12	0

Most observations were acquired during array reconfigurations (C→CnB; CnB→B; B→A). Horizontal lines denote changes in array configuration, as indicated by the changes in the synthesized beam size.

Extended Data Table 3 | Flux density and position measurements of the persistent counterpart to FRB 121102

Telescope	Frequency (GHz)	Flux density (μJy)	ΔRA (s)	ΔDec ($''$)
VLA	1.63	250 ± 39	0.694 ± 0.018	0.43 ± 0.26
	3.0	206 ± 17	0.705 ± 0.005	0.43 ± 0.07
	6.0	203 ± 7	0.701 ± 0.005	0.54 ± 0.01
	10.0	166 ± 9	0.701 ± 0.001	0.54 ± 0.02
	15.0	103 ± 7	0.691 ± 0.002	0.65 ± 0.02
	22.0	66 ± 7	0.699 ± 0.001	0.56 ± 0.01
VLA Weighted Average			0.6998 ± 0.0004	0.548 ± 0.006
EVN	1.67	200 ± 20	0.70150 ± 0.00003	0.5505 ± 0.0003
VLBA	1.55	218 ± 38	0.70159 ± 0.00002	0.5508 ± 0.0006
	4.98	151 ± 19	0.701530 ± 0.000003	0.54952 ± 0.00009
Gemini			0.69 ± 0.01	0.51 ± 0.10

We report the VLA radio spectrum with continuous frequency coverage from 1 GHz to 25 GHz, along with detection positions and a weighted-average position that is consistent with the detected burst positions to within 0.1″. We also list VLBA, EVN and Gemini detection positions. Position offsets ΔRA and ΔDec are measured from a nominal RA = 05 h 31 min 58 s, Dec = +33° 08′ 52″ (J2000). The Gemini r-band detection position is also included. 1σ errors are quoted in all cases.